High speed processing of $NiFe_2O_4$ spinel using a laser furnace

B. Özçelik [a], S. Özçelik [b], H. Amaveda [c], H. Santos [c], C.J. Borrell [c], R. Sáez-Puche [d], G.F. de la Fuente [c], L.A. Angurel [c, *]

[a] Çukurova University, Faculty of Sciences and Letters, Physics Department, 01330, Adana, Turkey
[b] Hakkari University, Engineering Faculty, Food Engineering Department, 30000, Hakkari, Turkey
[c] ICMA (CSIC-University of Zaragoza), María de Luna, 3, 50018, Zaragoza, Spain
[d] Department of Inorganic Chemistry, University Complutense of Madrid, 28040, Madrid, Spain

ABSTRACT

The Laser Furnace (LF) method has been applied to directionally solidify $NiFe_2O_4$ spinel disks from a mixture of Fe and Ni oxides in order to obtain uniform, dense targets for controlled synthesis of spinel nanoparticles via Laser Ablation. Application of a CO_2 laser in Line Scan mode onto a sample with the desired stoichiometry, enabled melt processing above 1580 °C at its outer surface layer. This process was carried out inside a continuous roller furnace at a maximum volume temperature of 1000 °C. Such combination helps avoid excessive thermal stress, crack formation and catastrophic failure of these magnetic ceramic monoliths. Higher energy incubation values yield increased molten volumes and a thicker resolidified surface layer with a dense microstructure. Despite the high solidification rates imposed, $NiFe_2O_4$ spinel is the main phase obtained according to X-Ray Diffraction (XRD) and magnetization studies. LF processed samples exhibit a reduction of the coercive fields and an increase of the saturation magnetization values, evidence for soft ferromagnetism and characteristic of the magnetic behaviour associated with this spinel. This work demonstrates the convenience of the LF method for preparation of uniform, dense targets for Laser Ablation and other evaporation based techniques used in the fabrication of nanoparticles.

1. Introduction

Iron based spinel ferrites with general formula $MeFe_2O_4$ (Me = Ni, Mn, Zn, Co, Cu, Mg, Cd) have recently gained considerable attention from the fundamental science point of view, both in bulk and nanoparticle form and as a result of their unique physical properties. They have thus been found promising for applications in such diverse areas as high-density data storage, magnetic media, microwave absorbers, ferro-fluids, catalysis, gas sensors, rechargeable lithium batteries, information storage systems, magnetic bulk cores, magnetic fluids (hyperthermia) and medical diagnostics and therapy, among others [1—9]. In addition, because of their very interesting magnetic behaviour, spinel ferrites are presently being considered in nanometric grain sizes for a number of applications in bioscience [10,11] such as, capping agents to deliver payloads (fertilizers, agrochemicals) into the specific location of fruit trees or high-input crops.

In the conventional crystallographic description of the spinel structure (space group *Fd3m*) oxygen anions distribute in a cubic close-packed array in which Me^{2+} and Fe^{3+} cations appear located in tetrahedral and octahedral lattice sites. Depending on the location of the cations, the structure may be described as normal or inverse spinel [12]. Nickel ferrite ($NiFe_2O_4$) is known to exhibit an inverse spinel structure, where the positions of the divalent cations (Ni^{2+}) are almost equivalent to their positions in the Nickel oxide structure [13], and it exhibits super-paramagnetic behaviour.

Inverse spinel $NiFe_2O_4$ ferrites are attractive magnetic semi-conducting materials because of their saturation magnetization (*Ms*) values and low coercivity, low eddy current losses and conductivity, combined with their high electrochemical stability [14—16]. For these reasons, they are considered for applications in sodium-ion batteries, wave absorption materials, dye removal by magnetic separation, electromagnetic wave absorption, enhancement of water oxidation processes, adsorption, photocatalysis, etc. [17—21].

Significant research efforts have addressed the preparation of $NiFe_2O_4$ spinel ferrites. In the past decade, various preparative routes for synthesizing spinel ferrites have been explored, including sol-gel, auto combustion, hydrothermal, elevated temperature and microwave-assisted methods [22–25]. All these techniques exhibit advantages and disadvantages from both, the efficiency and environmental points of view. The design of new synthesis methods for spinel ferrites, which pose a lower hazard and avoid the use of solvents and expensive precursor materials is thus a timely issue.

Laser Zone Melting (LZM) can be used as a densification process for different oxides at high rates and in situations that are not in equilibrium [26–29]. LZM provides a number of advantages, although until recently it was not possible to process large area samples under controlled solidification conditions. These are necessary in order to exert a good degree of microstructure control. High intensity laser irradiation of a surface produces high temperature gradients within the volume in proximity to the irradiated area, giving rise to extreme thermomechanical stress. When the process is carried out at room temperature, most ceramic materials are unable to withstand such stress and develop cracks. In many instances, these cracks propagate and cause uncontrolled shattering and loss of sample integrity. To reduce this effect, laser zone melting has been combined with a continuous roller furnace to perform these treatments at high sample volume temperatures [30,31]. This combined device, known as a Laser furnace, provides a scalable method to process ceramic materials in a continuous way and within the material's thermomechanical stress limits. The sample is introduced into a roller kiln, where a desired temperature gradient is defined and the thermal curve is controlled with several temperature zones and a predefined constant sample movement speed. When the sample reaches the maximum temperature zone, a laser beam is focused on the surface describing a line perpendicular to the sample movement direction. With this configuration, the laser beam scans the full sample surface in a uniform manner, inducing a stable melt line perpendicular to sample displacement.

This work reports on the potential use of the Laser Furnace technique to obtain dense $NiFe_2O_4$ monoliths at high speeds. Its aim is to develop a protocol for the preparation of laser ablation targets suitable for nanoparticle fabrication. Moreover, this work pretends to obtain ablation targets of the above materials with uniform chemical composition at their surface, rather than a high degree of texture. For this reason, moderately high laser processing speeds were used.

2. Experimental procedure

In order to obtain Nickel ferrite spinel ($NiFe_2O_4$), stoichiometric amounts of NiO (Sigma-Aldrich, 99.8%, d < 10 μm) and α-Fe_2O_3 (IROX-00T-500, 95–98%, H_2O solubility <1% Phosphate (PO_4) <0.3%, Manganese (Mn) < 0.25%, Sulfates (SO_4) <0.5%, d < 1 μm) were mixed and ball milled for 30 min at 300 rpm with distilled water, which was evaporated from the slurry by using infrared lamps. After drying, the resulting powders were manually milled and then pressed into 3 mm thick by 20 mm diameter pellets.

The laser treatment was performed using a previously reported method, known as laser line scanning [26]. Samples were introduced into a 4 m-long roller furnace (Nanetti model ER) at a traverse rate of 1500 mm/h. They were subjected to a thermal curve in which the maximum temperature, at the centre of the furnace, was set at 1000 °C [30,31]. The laser treatment was performed in the region with the maximum temperature by focusing a beam of a pulsed 350 W CO_2 laser (Rofin-Sinar Slab-type CO_2, UK) onto the sample surface. The laser operated at a pulsed repetition frequency of 20 kHz with a pulse width of 50 μs, emitting during a fraction of the pulse width, defined by a duty cycle. The laser focus was moved using an optical beam steering system at 15875 mm/s in order to transform the circular cross-section beam (0.8 mm in diameter) into a line measuring approximately 0.8 mm in thickness and the desired length in width (specified in Table 1).

Three samples, labelled as S1, S2 and S3, were prepared using the laser parameters recorded in Table 1. In the case of sample S1, a lower duty cycle value was used in comparison to the other two samples. The difference between the laser conditions used to process samples S2 and S3 is the length of the line covered by the laser, 70 mm in case of sample S2 and 50 mm in case of sample S3. For comparison purposes, a fourth characterised sample, S0, was merely annealed in the roller furnace with the same thermal treatment as the rest of the processed samples, but without the laser irradiation.

In order to evaluate the level of interaction of the laser with the surface of the sample, several parameters are herewith defined:

Irradiance: laser power per unit area irradiated and per pulse (W cm^{-2}), assuming only the time the laser is ON during a laser pulse period. Overlap between two consecutive pulses is not considered.

Energy Incubation per Line: Energy density provided by the laser during a period, taking into account the duty cycle and the overlap between consecutive pulses in the line scanned by the laser beam.

Line filling factor: Number of lines scanned by the laser per unit length advanced by the sample in the traverse direction.

Total Energy Incubation: Total energy deposited per unit area during the laser process taking into account the area covered by the laser along a line, the overlap between consecutive pulses, the length of the scanned laser line and the overlap between successive laser lines in the traverse direction.

The irradiance provides information about the effect of only one pulse. The Energy Incubation per line describes effects associated with incubation energy when the laser scans only one line. Finally, the Total Energy Incubation represents the total energy input during the complete laser irradiation cycle. All these parameters have been recorded in Table 1 for the three samples studied. In comparison to the values used for processing sample S1, the Total Energy Incubation, for example, is 23% higher for sample S2 and 73% higher for sample S3.

Microstructural characterization was performed using field emission scanning electron microscopy (FESEM) and X-ray diffractometry (XRD). Surface and cross-section FESEM studies were performed using a Carl Zeiss MERLIN microscope operating at 15 kV, with a spatial resolution of 0.8 nm. Semi-quantitative elemental analyses were carried out using an energy dispersive X-ray detector (EDX). Additional EBSD studies were also performed in order to identify spinel phase single grains in the samples after the laser treatment and possible grain orientation induced during the laser process. X-ray diffraction patterns were recorded at room temperature using a "D-max Rigaku, Ru300" diffractometer with a rotating anode. Measurements were performed at 40 kV and 80 mA using a Cu anode and a graphite monochromator, in order to select the CuKα radiation, and at a constant 2θ scan rate (0.03°/s) in the 10°-80° range. Crystalline phases were identified using the "JCPDS-International Centre for Diffraction Data-2000" data base. Magnetization measurements were carried out on prismatic geometry samples, obtained from the central part of the processed pellets, in a Lake Shore 7304 model Vibrating Sample Magnetometer operating between 15 and 300 K. The magnetic field was applied perpendicular to the side of the sample that was treated with the laser.

Table 1
Laser parameters used to process samples S1, S2 and S3.

Sample	Dutty cycle (%)	Peak Laser Power (W)	Energy per pulse (mJ)	Average Laser Power (W)	Length of Laser line (mm)	Irradiance (kW/cm^2)	Energy Incubation per Line (J/cm^2)	Line filling factor (lines/mm)	Total Energy Incubation (J/cm^2)
S1	40	737,5	14,75	295	70	97.5	1,55	544	60,5
S2	50	700	17,50	350	70	85.4	1,91	544	70,6
S3	50	700	17,50	350	50	85.4	1,91	762	104,5

3. Results and discussion

3.1. Microstructure and XRD analysis

Fig. 1 shows the cross-sections of the three laser processed samples. These confirm the effect of the Total Energy Incubation onto the material surface. Sample S1 exhibits the thinnest molten section at its surface (ca. 20 μm), compared to S2 (ca. 80 μm) and S3 (ca. 170 μm), as observed respectively in Fig. 1 a-c, in accordance with increasing laser treatment strength. An interesting aspect of the laser induced re-melted layer is observed in sample S3, where the outer surface clearly seals the now internal porosity observed in all samples. This has already been reported for porcelain type ceramics, and may pose advantages towards chemical and environmental resistance of these samples, making them more robust against degradation under ambient conditions in the atmosphere [31]. Finally, from the micrographs of Fig. 1 it is reasonable to say that the size of pores increases when Total Energy Incubation, and, in consequence, the molten volume increase, as observed clearly in Fig. 1c.

The micrographs shown in Fig. 2 correspond to a detail of the cross-section of samples S1, S2 and S3, close to the surface that has been treated with the laser. The major phase observed in the three cases is the spinel, identified as the dark grey contrast in the images. The composition of this phase, determined by EDS, is lower than the stoichiometric one, with a ratio Ni/(Ni+Fe) in the range between 0.27 and 0.30 in samples S2 and S3, and slightly lower (0.24–0.29) in sample S1. A matrix with a lighter contrast and an intragranular dendritic structure forms the microstructure of this secondary phase. EDS analysis indicates that the above matrix has a
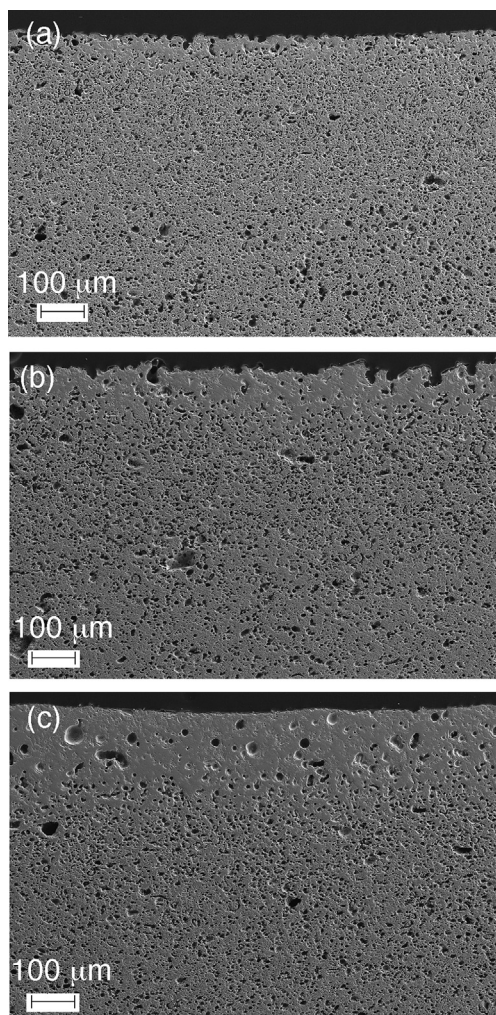

Fig. 1. Aspect of the cross-sections of samples S1 (*a*), S2 (*b*) and S3(*c*) after laser furnace treatment.
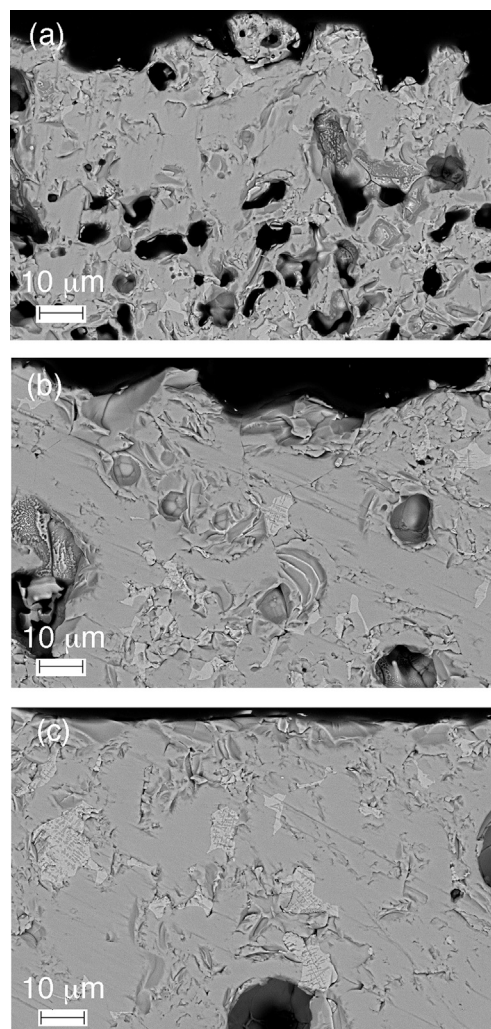

Fig. 2. Detail of the upper part of the cross-section of samples (*a*) S1, (*b*) S2 and (*c*) S3.

Ni-rich composition in which the Ni/(Ni+Fe) ratio reaches values between 0.72 (sample S3), 0.80 (sample S2) and 0.83 (sample S1). These may be associated with bunsenite, (Ni,Fe)O. Although the melting and solidification process induced by the laser is far from equilibrium conditions, this behaviour can, nevertheless, be understood following the trends observed in the equilibrium phase-diagram of the Fe—Ni—O system [32]. In this diagram, when the temperature increases above 1200 °C, the composition of the Fe—Ni spinel moves toward higher Fe concentrations with values of the Ni/(Ni+Fe) ratio falling below the theoretical one of 0.33. With this composition, the material enters into a region containing two phases, spinel and bunsenite. As the sample is obtained from a liquid phase, eutectic grains are expected to appear during solidification. It has been observed (see supplementary material Figures Sup1 and Sup2) that the amount of eutectic grains is higher approaching the surface, and decreases when the analysis is performed penetrating deeper inside the sample. In the case of sample S2, the volume percentage of the eutectic grains is around 4.7 ± 1.6 %vol in the 100 μm region closest to the surface. It decreases down to 2.3 ± 0.4 %vol if the analysis is performed at a depth of 200 μm from the surface. For sample S3, analysis close to the surface indicates an increased average grain size for this secondary phase, as well as amounts reaching approximately 9.5 ± 0.8 %vol. This value decreases within the inner region to 5.7 ± 0.6 %vol. Although these percentages are lower than expected from the equilibrium phase diagram, they seem reasonable considering that the high solidification rates used during the LF process are expected to produce samples which are far from equilibrium conditions. EBSD measurements (see supplementary material Figure Sup3) also show that these solidification rates do not generate texture in sample S2.

Fig. 3 shows the surface appearance of the three samples after laser processing. In correspondence with the cross-sections, these micrographs suggest that the main difference between samples S1 (Fig. 3a) and S2 (Fig. 3b) with respect to sample S3 (Fig. 3c) is that, in the latter, the solidification process from the melt has occurred within a complete surface layer, yielding a very flat surface with a much lower degree of porosity. In contrast, samples S1 and S2 exhibit a surface with higher roughness and a higher level of open porosity. The very thin molten layer in sample S1 results in very similar porosity and surface roughness to samples that have not undergone melting. In contrast, the larger size porosity generated within sample S2 in the molten region, reaches its outermost layers and induces higher surface roughness. In the case of sample S1, it is also important to point out that the structure of the surface is less uniform than in the other two samples. For instance, in Fig. 3a, the central region is different from that on the right side.

These differences are more evident under observation of the surface at higher magnification and compared with sample S0 (Fig. 4). Observation of the micrographs shown in this figure reveals at least two types of grain morphologies: smaller acicular phases appear deposited or grown on the surface of large grains, which seem to form an apparently uniform polycrystalline microstructure. EDX analysis suggests that the larger grains have a chemical composition very close to that of the spinel, while the acicular phase is associated to bunsenite. The surface roughness is quite different for samples S2 (Fig. 4a) and S3 (Fig. 4b). Following the trends that were also observed in Fig. 3, a relevant difference between these two samples is their level of porosity. Sample S2 exhibits large pores (Fig. 4a) near its surface, while sample S3 appears with low porosity and a highly compacted granular structure (Fig. 4b). The effect of the laser treatment is clearly observed if we compare these microstructures with the aspect of sample S0, shown in Fig. 4c. Combining these observations with the EBSD measurements (Fig Sup3) it was determined that the average grain size in sample S2 is within the range 10—25 μm. The latter increases
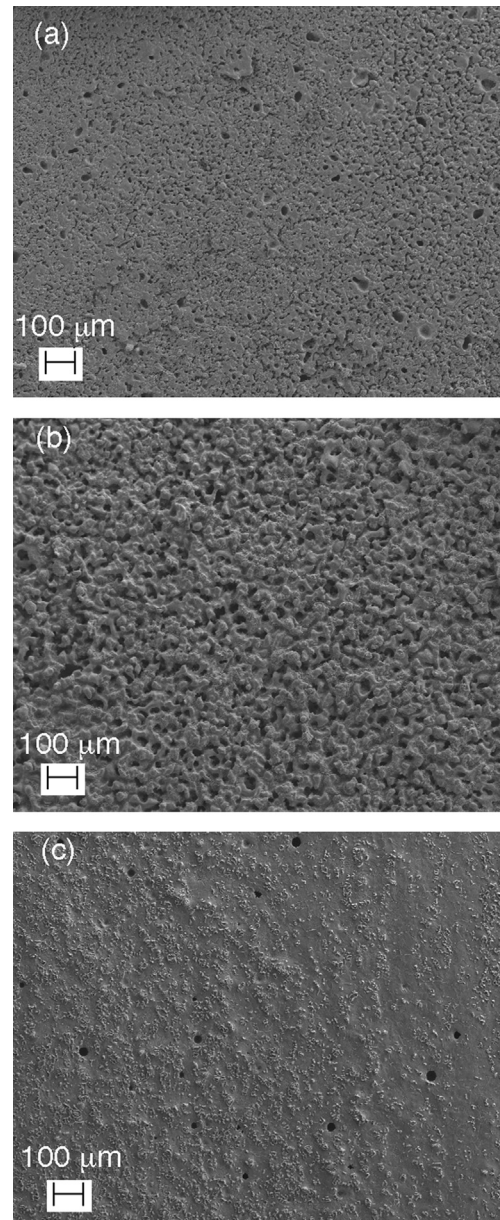

Fig. 3. FESEM micrographs of the surface of samples S1 (*a*), S2 (*b*) and S3(*c*) after laser furnace treatment.

to 20—60 μm for sample S3. In contrast, the reference sample S0 appeared to contain a mixture of granular phases, most of them in the submicrometer range and, in some cases, partially agglomerated. In this original sample, The transformation of the NiO and Fe_2O_3 mixture into $NiFe_2O_4$ has already started via solid state reaction for sample S0, as confirmed with the XRD analysis discussed later in the text. The evidence for partial transformation to the $NiFe_2O_4$ phase is consistent with the fact that this sample was furnace processed without laser irradiation at 1000 °C, temperature at which previous studies [33] confirmed that this transformation has already started.

Moreover, visible grain junctions are clearly observable within the nearly flat grain structure of sample S3 (Fig. 4b) and in some regions of sample S2. It is also curious that the solidified structures observed in these samples exhibit the unique microstructure appearing in the micrograph shown in Fig. 5. The junctions appear
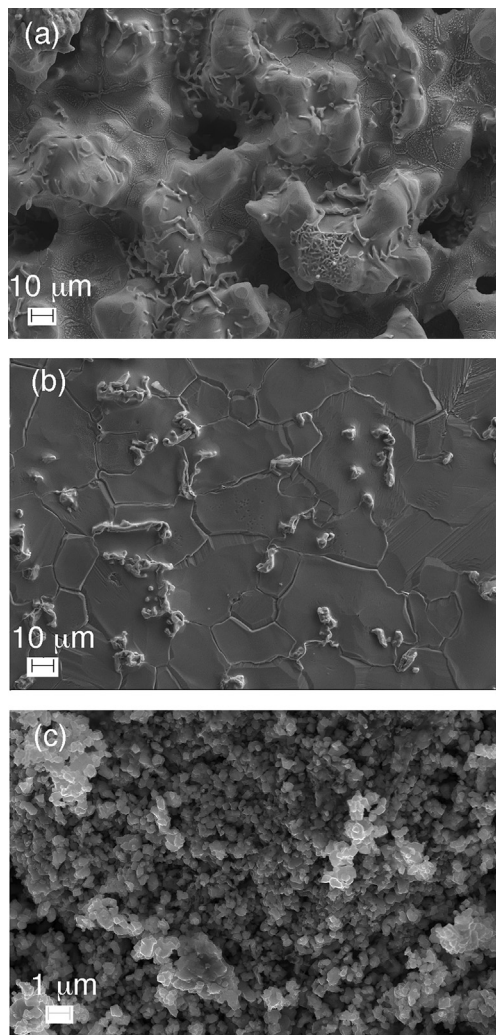
Fig. 4. Detail of the surface of samples S2 (**a**), S3 (**b**) and S0 (**c**).
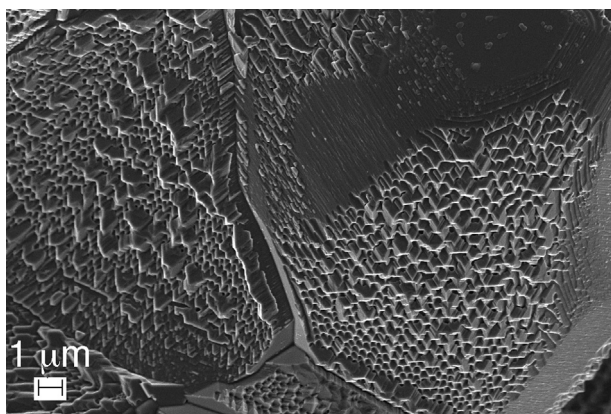

Fig. 5. Microstructure observed around grain boundaries in sample S3.

to grow vertically at an angle out of the plane, indicating an appreciable rate of growth in an outward dimension with respect to the directional-solidification-driven grain growth within the plane. This grain growth habit is tubular with square or rectangular cross-section, thus yielding a surprising microstructure where grains are linked through the long walls and highly aligned in a preferential
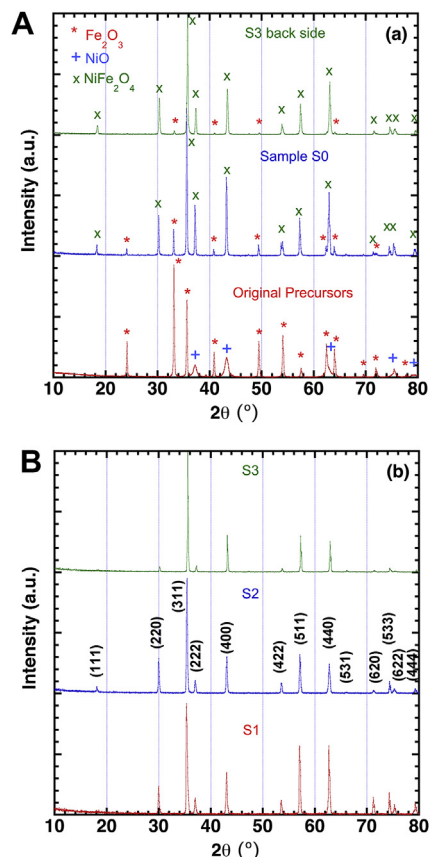

Fig. 6. XRD-patterns of samples, (**a**) non-irradiated with the laser, (**b**) laser furnace processed.

direction within each large grain. These reach a limit at the grain boundaries, where different growth habit directions meet.

XRD patterns of the samples in different steps of the processing protocol are presented in Fig. 6. Fig. 6a shows the XRD patterns corresponding to the original mixture of oxides, for samples S0 and S3 on the face that was not irradiated with the laser. As mentioned in the SEM discussion, the transformation of the initial oxides into $NiFe_2O_4$ had already started for sample S0. The main diffraction lines associated with Fe_2O_3 are also visible for this sample, however, indicating that the transformation of the starting Ni and Fe oxides into $NiFe_2O_4$ is not yet complete. Here, the diffraction lines for NiO are not distinguishable, because they appear in the same positions as the main lines of the spinel structure. The transformation of the original component mixture into the spinel structure is neither completed on the opposite face of the laser irradiated S3 sample, which has been treated with the highest Total Energy Incubation.

In contrast, the transformation into single phase $NiFe_2O_4$ is completed on the three faces that have been treated with the laser, where only the diffraction lines associated with the spinel phase are detected. These lines have been indexed to the corresponding crystallographic planes, as shown in Fig. 6b. The crystal symmetry of all samples was determined as cubic with the space group $Fd3m$. Each diffraction line observed in Figure Sup4 (supplementary material) exhibits two maxima separated by approximately 0.12°. This can be associated to the fact that the spinel grains do not have a fixed composition, as observed by EDS. Small changes in the Ni/(Ni+Fe) ratio produce small changes in the crystal lattice parameters. These were calculated using the least squares method as 8.35(3) Å in S3, and 8.42(2) Å in the other two laser treated samples,

in agreement with the values reported in the literature [34,35].

Furthermore, sample S3 exhibits a diffraction pattern where the identified lines appear with different relative intensities when compared to the other samples studied. These are expected from the induced texture typically associated to the Zone Melting process carried out. The laser furnace conditions imposed on this sample generate a stationary molten line, which travels at constant speed through the sample's length. The sharp solidification interface defined by the melt yields a directionally solidified microstructure, which should exhibit some tendency towards preferential grain alignment. This is likely responsible for the change in relative intensities observed in XRD experiments for sample S3 (see supplementary material, Figure Sup5). EBSD observation in SEM was carried out on transversal sections of the samples with the aim of ascertaining grain size distribution, and do not necessarily correlate with possible texture observed in XRD, as the latter measurements were carried out on the samples' surfaces. Nevertheless, the degree of texture is not as obvious in this cubic crystallographic system, as it is in a structurally anisotropic solid. This has been demonstrated with BSCCO superconductors [26,28], for example. However, an important difference with respect to processing of highly textured materials by Laser Zone Melting must be taken into account. That is referred to the traverse rate, which is about two orders of magnitude faster in the present case (1500 mm/h) when compared to well textured superconductors (30 mm/h). The latter could be a reason not to observe a microstructure of highly aligned, large grains for the spinel phase reported here.

3.2. Magnetic behaviour

In order to understand the magnetic nature of Ni spinel ferrite generated without and with the laser treatment, zero-field-cooled (ZFC) magnetization profiles were obtained between 15 and 300 K. In ZFC mode, the sample was cooled from 300 K down to 15 K in the absence of a magnetic field. At 15 K, a magnetic field of 50 Oe was applied and the magnetization was recorded while the temperature was increased from 15 to 300 K. Fig. 7 shows the ZFC magnetization curves obtained for the four samples reported here. All ZFC magnetization curves obtained on laser treated samples exhibit a broad maximum centred at a given temperature. It may be argued that when NiFe$_2$O$_4$ spinel is cooled to low temperature (15 K) in the absence of an external magnetic field, the magnetic moments in
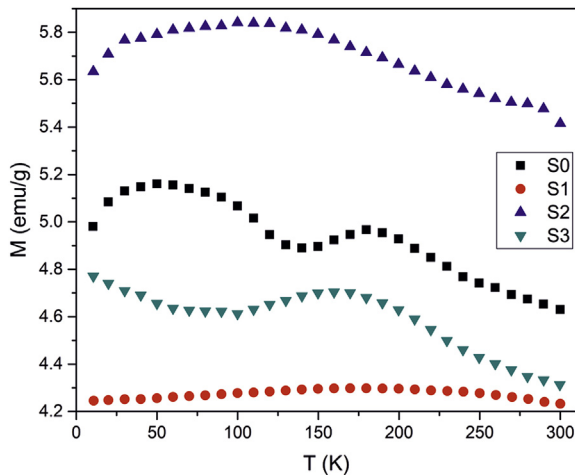
each single-domain start to align along their easy axis to reach a local minimum of potential energy. At this stage, the individual magnetic anisotropy of particles acts as an energy barrier to prevent the magnetization direction from switching away from the easy axis. When the temperature starts to increase from 15 K, the magnetization directions of thermally activated particles begin to align with the applied magnetic field, resulting in an initial increment of the total magnetization. When a certain temperature is achieved, the magnetic anisotropy energy barrier is surpassed by thermal activation and the magnetization direction of the particles begins to fluctuate, revealing a super-paramagnetic behaviour [36]. This temperature is associated with the perturbation of magnetic anisotropy energy by thermal energy, and presents a broad maximum in the ZFC magnetization curve, known as the blocking temperature T_B [37]. In addition, for sample S0, a re-entrant magnetic behaviour is observed. At lower temperatures, magnetization starts to increase and passes from a broad maximum around 50 K, due to the hematite α-Fe$_2$O$_3$ impurities embedded in the matrix, to initially reach a minimum, known as the compensation point and observed around $T_{comp} = 125$ K. Finally, a broad transition takes place at around $T_B = 150$ K. Such behaviour may be closely related to the existence of a magnetically disordered surface layer, in which direct competition of exchange interactions between surface spins takes place. In addition, the origin of magnetic disorder may arise from a lack of crystallinity, uncompensated magnetic interactions of the surface spins, the existence of some randomly oriented grains having different sizes and/or disordered vacancies.

Finally, it can be emphasized that S0 and S3 samples exhibit similar magnetic behaviour, except for a low temperature peak. At the low temperature region, while sample S0 undergoes a magnetic phase transition, sample S3 does not, apparently as a consequence of the laser treatment. Directional solidification may induce, in the latter case, microstructural changes which result in new grain junctions providing a barrier for magnetic domain movement. It is important to emphasize here that, in sample S1, the temperature dependence of the magnetization is very small, with a difference between the maximum and the minimum value of around 0.05 emu/g. This is 10 times smaller than in samples S2 and S3. In addition, an increase in Total Energy Incubation results in an increase in the magnetization value, with its maximum becoming broader for sample S2. For sample S3, the magnetization magnitude starts to decrease and exhibits an increase at low temperatures. In this sample, processed using the highest Total Energy Incubation, a larger volume of surface molten material has been generated and higher temperatures have apparently been reached, particularly at the proximity of the incident laser line.

Fig. 8 represents the magnetization behaviour as a function of magnetic field intensity at 10 and 300 K, respectively, recorded within the ±10 kOe range for the reference sample (S0), as well as for the three samples prepared via de Laser Furnace method (S1−S3). The corresponding magnetization parameters are summarized in Table 2. The magnetic field dependence of the magnetization, M, near the saturation magnetization is expressed as follows [38,39]:

$$M = M_S[1 - \frac{\beta}{H^2}]$$

where M_s is the saturation magnetization, β is related with the magneto-crystalline anisotropy and H is the applied magnetic field. By plotting M versus $1/H^2$, β and M_s values are obtained from the slope of the linear fitting and from the y-axis intercept, respectively. Fig. 9 shows this dependence at both temperatures.

The M_s values for sample S0 (29.7 and 34.7 emu/g at temperatures of 300 and 10 K, respectively) are always lower than those of
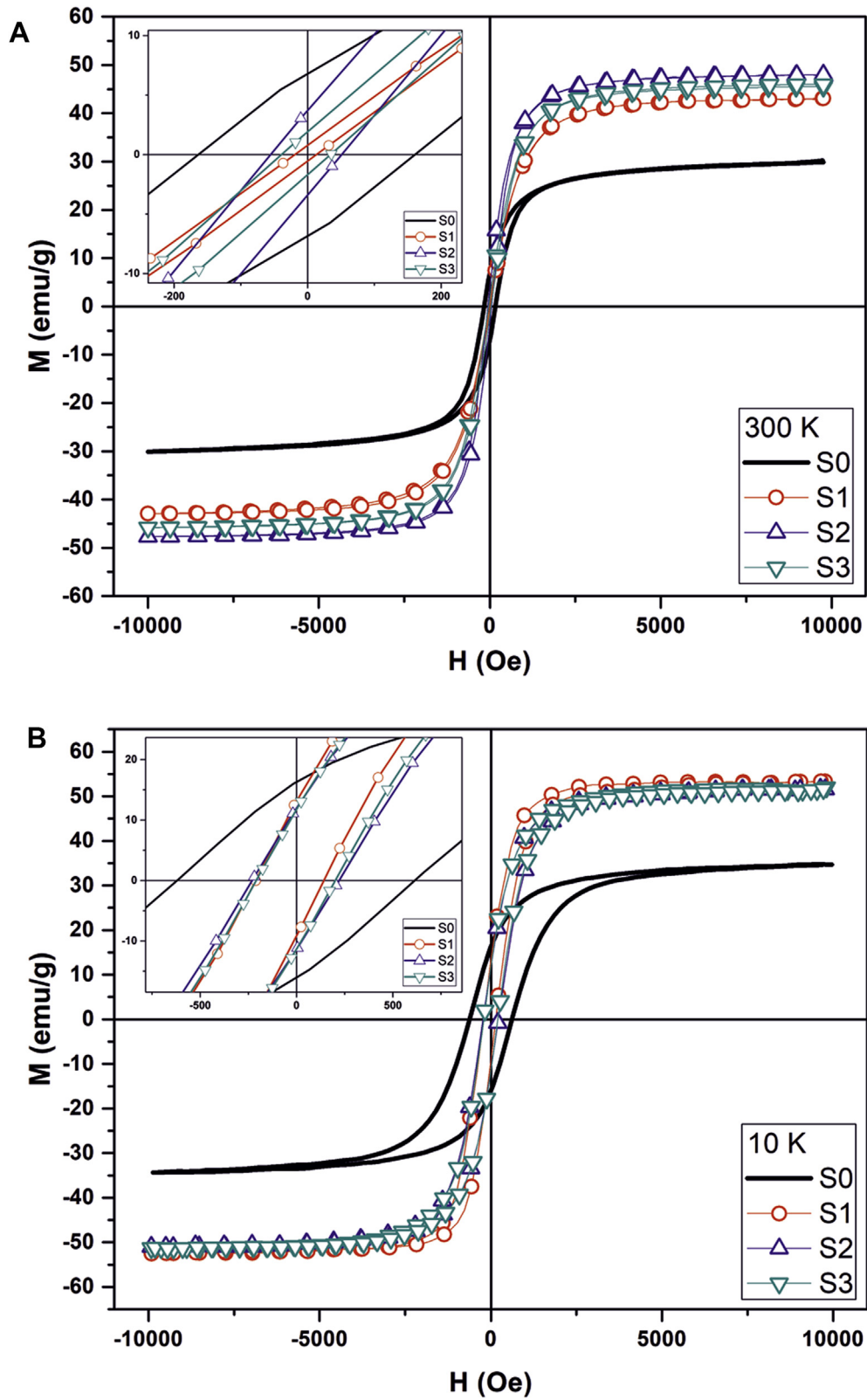

Fig. 7. ZFC magnetization curves measured under an applied magnetic field of 50 Oe in the four samples.

Fig. 8. Magnetic hysteresis loops measured at (**a**) 300 and (**b**) 10 K. Inserts show the enlarged axis in order to better observe the coercive field values.

the samples prepared using the Laser Furnace technique. This can be explained by the fact that the spinel reaction has not yet been completed in this sample, implying that the presence of α-Fe_2O_3 and NiO phases with lower magnetization values [40] is significant.

On the other hand, the three samples (S1–S3) that have been treated with the laser exhibit a very similar behaviour, with saturation values close to those measured in bulk Spinel samples, approaching values of 50 and 56 emu/g at 300 and 10 K,

Table 2
Values of the saturation magnetization, the coercive fields and the β-parameters at 10 and 300 K for the four samples subjected to study in this work.

Sample	10 K			300 K		
	M_s (emu/g)	H_c (Oe)	β ($Oe^2 \times 10^7$)	M_s (emu/g)	H_c (Oe)	β ($Oe^2 \times 10^7$)
S0	34.8	618	3.2	29,7	168	3.1
S1	53.7	142	2.5	43,2	13	2.6
S2	51.9	224	2.8	48,2	52	1.9
S3	52.4	201	2.7	45,6	36	2.1

respectively [12]. It is important to emphasize that estimated M_s values are very close to the values of M measured with H = 10 kOe, indicating that the applied field is large enough to reach the saturation values of the samples synthesized in the present study. S1 exhibits the highest value of M_s amongst all samples. This can be understood taking into account the Fe-rich composition of the spinel phase that has been measured by EDX in the three samples. In sample S1 the ratio Fe/Ni = 2.7(2), while in S2 and in S3 it becomes Fe/Ni = 2.6(2). Considering that the excess of Fe stems from the substitution of Ni^{2+} cations (magnetic moment $2\mu_B$) by Fe^{3+} cations (magnetic moment $5\mu_B$) in the octahedral positions of the structure, these differences in stoichiometry increase the magnetic moment of the material. With these assumptions, it is expected that the increase of the magnetic moment per molecule is of the order of 0.1 μ_B/f.u., which is equivalent to approximately 2 emu/

cm^3. This value is similar to the differences that have been measured in the M_s values in the three laser-processed samples, suggesting that they can be associated to the changes in stoichiometry of the spinel phase in these samples. The temperature dependence of M_s is strongly affected by the interaction between both magnetic sublattices [12]. As the change in the Spinel stoichiometry induces small changes in the magnetic sublattices, it is expected that the temperature dependence can be slightly different in the three samples, a fact that has been observed comparing their magnetic behaviour at 10 K and 300 K. The magnetic loops show a very narrow S-shape hysteresis, with low coercive field values (see insets in Fig. 8 and Table 2), evidence for soft ferromagnetism. As can be gathered from Table 2, the coercive field (H_c) value measured in sample S2 is larger than in sample S3. The reason for this decrease may be attributed mainly to an increment of the grain size. As already mentioned above (see Fig. 4), sample S3 contains larger grains than S2. It is well accepted that larger grains tend to consist of a greater number of domain walls. The energy required for domain wall movement is lower than for domain rotation. In this case, while the number of walls increases with grain size, the contribution of wall movement to magnetization becomes greater than that of domain rotation. Therefore, it is expected that samples having larger grains will have lower coercive H_c values [33].

4. Conclusions

This work presents, for the first time, the application of the continuous Laser Furnace (LF) technique to obtain $NiFe_2O_4$ spinel from a starting mixture of Fe and Ni oxides. It reports the facile and fast preparation of dense, uniform spinel monoliths. Because the LF method combines continuous laser line scan melting with sample volume soaking at high temperatures, this works demonstrates that it is feasible to obtain highly densified, resolidified ceramic surfaces in a scalable fashion, without cracks or shattering. This may be of significant practical interest, since these magnetic phases, as well as ceramics in general, are prone to thermal shock when laser processed, due to the intense thermomechanical stress intrinsic to focused laser irradiation. Taking into account the results reported here, the Total Energy Incubation is found to be the most influential parameter towards control of the laser furnace process herein presented. XRD and Magnetization measurements confirm the transformation of the original Ni and Fe oxide pressed powder mixture into a dense monolith with the resultant Ni–Fe–O spinel structure after continuous LF processing. These dense, uniform LF products can further be used, in principle, as ideal targets for the fabrication of $NiFe_2O_4$ nanoparticles using laser ablation processes.

Declaration of competing interest

The authors declare that they have no known competing financial interests or personal relationships that could have appeared to influence the work reported in this paper.
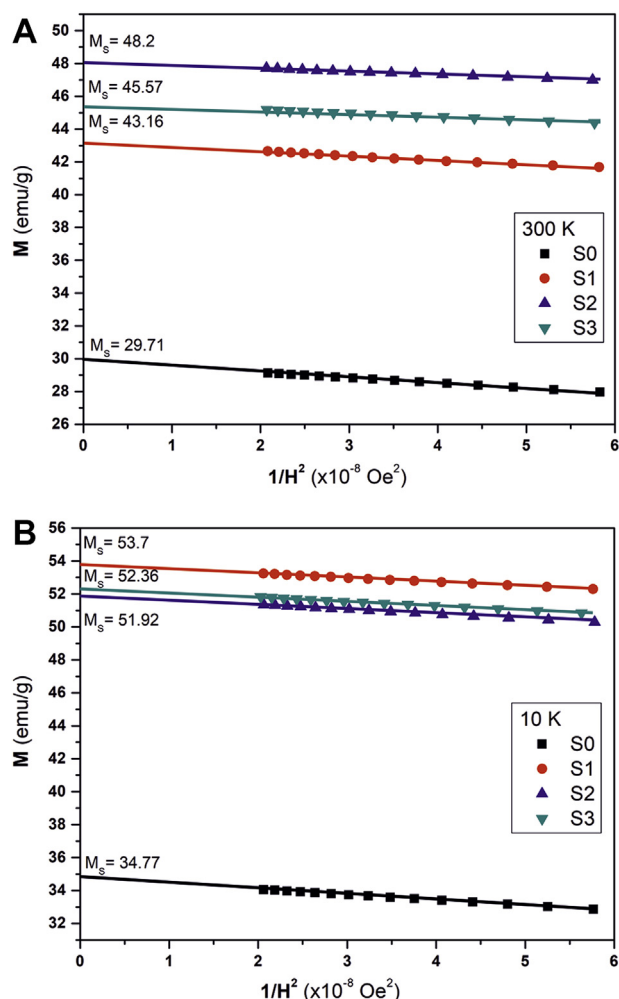

Fig. 9. Plots of M against 1/H^2 at (**a**) 300 K and (**b**) 10 K.

Appendix A. Supplementary data

Supplementary data to this article can be found online at https://doi.org/10.1016/j.jmat.2020.05.003.

References

[1] Ahmed YMZ, Ewais EMM, Zaki ZI. In situ synthesis of high density magnetic ferrite spinel ($MgFe_2O_4$) compacts using a mixture of conventional raw materials and waste iron oxide. J Alloys Compd 2010;41(12):269—74.

[2] Lin KS, Adhikari AK, Wang CY, Hsu PJ, Chan HY. Synthesis and characterization of nickel and zinc ferrite nanocatalysts for decomposition of CO_2 greenhouse effect gas. Catal Today 2011;174(1):88—96.

[3] Tyagi S, Baskey HB, Agarwala RC, Agarwala V, Shami TC. Development of hard/soft ferrite nanocomposite for enhanced microwave absorption. Ceram Int 2011;37(7):2631—41.

[4] López J, González-Bahamón LF, Prado J, Caicedo JC, Zambrano G, Gómez ME, Esteve J, Prieto P. Study of magnetic and structural properties of ferrofluids based on cobalt-zinc ferrite nanoparticles. J Magn Magn Mater 2012;324(4):394—402.

[5] Yan Z, Gao J, Li Y, Zhang M, Gao M. Hydrothermal synthesis and structure evolution of metal-doped magnesium ferrite from saprolite laterite. RSC Adv 2015;5:92778—87.

[6] Olsson RT, Salazar-Alvarez G, Hedenqvist SM, Gedde UW, Lindberg F, Savage SJ, et al. Controlled synthesis of near- stoichiometric cobalt ferrite nanoparticles. Chem Mater 2005;17:5109—18.

[7] Latham AH, Williams ME. Controlling transport and chemical functionality of magnetic nanoparticles. Acc Chem Res 2008;41:411—20.

[8] Moussaoui HE, Mahfoud T, Habouti S, El Maalam K, Ben Ali M, Hamedoun M, Mounkachi O, Masrour R, Hlil EK, Benyoussef A. Synthesis and magnetic properties of tin spinel ferrites doped manganese. J Magn Magn Mater 2016;405:181—6.

[9] Mathew DS, Juang R. An overview of the structure and magnetism of spinel ferrite nanoparticles and their synthesis in microemulsions. Chem Eng J 2007;129:51—65.

[10] Elayakumar K, Manikandan A, Dinesh A, Thanrasu K, Raja KK, Kumar RT, Slimani Y, Jaganathan SK, Baykal A. Enhanced magnetic property and anti-bacterial biomedical activity of Ce^{3+} doped $CuFe_2O_4$ spinel nanoparticles synthesized by sol-gel method. J Magn Magn Mater 2019;478:140—7.

[11] Sonia MML, Anand S, Blessi S, Pauline S, Manikandan A. Effect of surfactants (PVB/EDTA/CTAB) assisted sol-gel synthesis on structural, magnetic and dielectric properties of $NiFe_2O_4$ nanoparticles. Ceram Int 2018;44:22068—79.

[12] Smit J, Wijn HPJ, Ferrites. Philips technical library. The Netherlands: Cleaver-Home Press Ltd; 1959.

[13] Sagadevana S, Chowdhury ZZ, Rafique RF. Preparation and characterization of nickel ferrite nanoparticles via Co-precipitation method. Mater Res 2018;21(2):e20160533.

[14] Joshi S, Kumar M, Chhoker S, Srivastava G, Jewariya M, Singh VN. Structural, magnetic, dielectric and optical properties of nickel ferrite nanoparticles synthesized by co-precipitation method. J Mol Struct 2014;1076:55—62.

[15] Alarifi A, Deraz NM, Shaban S. Structural, morphological and magnetic properties of $NiFe_2O_4$ nano-particles. J Alloys Compd 2009;486:501—6.

[16] Padmapriya G, Manikandan A, Krishnasamy V, Jagana-than SK, Antony SA. Spinel $Ni_xZn_{1-x}Fe_2O_4$ ($0.0 \leq x \leq 1.0$) nano- photocatalysts: synthesis, characterization and photocatalytic degradation of methylene blue dye. J Mol Struct 2016;1119:39—47.

[17] Zhu H, Jiang R, Qian Y, Li FR, Yao J, Jiang S. Novel multi- functional $NiFe_2O_4$/ZnO hybrids for dye removal by adsorption, photocatalysis and magnetic separation. Appl Surf Sci 2016;369:1—10.

[18] Wu F, Wang X, Xu MLH. A high capacity $NiFe_2O_4$/RGO nanocomposites as superior anode materials for sodium-ion batteries. Ceram Int 2016;42:16666—70.

[19] Yan J, Huang Y, Chen X, Wei C. Conducting polymers- $NiFe_2O_4$ coated on reduced graphene oxide sheets as electromagnetic (EM) wave absorption materials. Synth Met 2016;221:291—8.

[20] Chen H, Yan J, Wu H, Zhang Y, Liu S. One-pot fabrication of $NiFe_2O_4$ nanoparticles on α-Ni(OH)$_2$ nanosheet for enhanced water oxidation. J Power Sources 2016;324:499—508.

[21] Manikandan A, Hema E, Durka M, Seevakan K, Alagesan T, Antony SA. Room temperature ferromagnetism of magnetically recyclable photocatalyst of $Cu_{1-x}Mn_xFe_2O_4TiO_2$ ($0.0 \leq x \leq 0.5$) nano-composites. J Supercond Nov Magnetism 2015;28:1783—95.

[22] Tahir MB, Iqbal T, Hassan A, Ghazal S. Wet chemical co- precipitation synthesis of nickel ferrite nanoparticles and their characterization. J Inorg Organomet Polym 2017;27:1430—8.

[23] Li H, Wu HZ, Xiao GX. Effects of synthetic conditions on particle size and magnetic properties of $NiFe_2O_4$. Powder Technol 2010;198:157—66.

[24] Li DY, Sun YK, Gao PZ, Zhang XL, Ge HL. Structural and magnetic properties of nickel ferrite nanoparticles synthesized via a template-assisted sol—gel method. Ceram Int 2014;40:16529—34.

[25] Parishan M, Nadafan M, Dehghani Z, Malekfar R, Khorrami GHH. Optical and dielectric properties of $NiFe_2O_4$ nanoparticles under different synthesized temperature. Results Phys 2017;7:3619—23.

[26] Lennikov VV, Özkurt B, Angurel LA, Sotelo A, Özçelik B, de la Fuente GF. Microstructure and transport properties of Bi-2212 prepared by CO_2 laser line scanning. J Supercond Nov Magnetism 2013;26:947—52.

[27] Larrea A, de la Fuente GF, Merino RI, Orera V. ZrO_2-Al_2O_3 eutectic plates produced by laser zone melting. J Eur Ceram Soc 2002;22:191—8.

[28] Mora M, Lennikov VV, Amaveda H, Angurel LA, de la Fuente GF, Bona MT, Mayoral C, Andrés JM, Sánchez-Herencia J. Fabrication of superconducting coatings on structural ceramic tiles. IEEE Trans Appl Supercond 2009;19:3041—4.

[29] de Francisco I, Lennikov VV, Bea JA, Vegas A, Carda JB, de la Fuente GF. In-situ laser synthesis of rare earth aluminate coatings in the system Ln-Al-O (Ln=Y, Gd). Solid State Sci 2011;13:1813—9.

[30] Estepa LC, de la Fuente Leis GF. Continuous furnace with coupled laser for the surface treatment of materials. US Patent 20090230105; 2009EP1992445 (2008), Continuous Method for the Surface Treatment of Materials, China patent No. ZL 2012100224412. Filing date: March 6, 2007, Published date: March 26, 2014.

[31] Rey-García F, Gutiérrez-Mora F, Borrell CJ, Estepa LC, Angurel LA, de la Fuente GF. Microstructural characterization and tribological behavior of Laser Furnace processed ceramic tiles. Ceram Int 2018;44:6997—7005.

[32] Rhamdhani MA, Hayes PC, Jak E. Subsolidus phase equilibria of the Fe-Ni-O systemm. Metall Mater Trans B 2008;39:690—701.

[33] Zabotto FL, Gualdi AJ, Eiras JA, Aparecido AJ, García D. Influence of the sintering temperature on the magnetic and electric properties of $NiFe_2O_4$ ferrites. Mater Res 2012;15:428—33.

[34] Asiri S, Sertkol M, Güngünes H, Amir Md, Manikandan A, Ercan I, Baykal A. The temperature effect on magnetic properties of $NiFe_2O_4$ nanoparticles. J Inorg Organomet Polym Mater 2018;28:1587—97.

[35] Ponpandian N, Balaya P, Narayanasamy A. Electrical conductivity and dielectric behaviour of nanocrystalline $NiFe_2O_4$ spinel. J Phys: Condens Matter 2002;14:3221—37.

[36] Lu AH, Salabas EL, Schuth F. Magnetic nanoparticles: synthesis, protection, functionalization, and application. Angew Chem Int Ed 2007;46:1222—44.

[37] Liu C, Zou B, Rondinone AJ, Zhang ZJ. Reverse micelle synthesis and characterization of superparamagnetic $MnFe_2O_4$ spinel ferrite nanocrystallites. J Phys Chem B 2000;104:1141—5.

[38] Topkaya R, Akman Ö, Kazan S, Aktas B, Durmus Z, Baykal A. Surface spin disorder and spin-glass-like behaviour in manganese-substituted cobalt ferrite nanoparticles. J Nanoparticle Res 2012;14:1156.

[39] Fang HC, Yang Z, Ong CK, Li Y, Wang CS. Preparation and magnetic properties of (Zn-Sn) substituted barium hexaferrite nanoparticles for magnetic recording. J Magn Magn Mater 1998;187:129—35.

[40] Islam MS, Kurawaki J, Kusumoto Y, Abdulla-Al-Mamum M, Bin Mukhlish MZ. Hydrothermal novel synthesis of neck-structured hyperthermia-suitable magnetic (Fe_3O_4, γ-Fe_2O_3 and α-Fe_2O_3) nanoparticles. J Sci Res 2012;4:99—107.

Prof. Bekir Özçelik has recieved his MSc and PhD degrees from Çukurova University (Adana-Turkey), completing the experimental part of his PhD thesis, related to harmonic and non-harmonic susceptibilities of various magnetic materials as anti-, ferro-magnetic and spin-glasses, at the Kamerlingh Onnes Laboratory (Leiden University-Holland) between 1988 and 1990. He currently holds a position as Professor at Çukurova University. His research work deals with High Tc superconductors, thermoelectrics, magnetic and nano materials. He keeps intensive scientific collaborations with the University of Zaragoza in Spain and the National Institute for Materials Science (NIMS) at Tsukuba-Japan. He has published more than 90 peer-reviewed journal articles and 4 problem solution books in Mathematics.

Dr. Sezen Özçelik is working as an Assistant Professor at the Food Engineering Department of Hakkari University in Turkey. She completed her undergraduate education at the Faculty of Fisheries and the Biology Department (minor program), Faculty of Science at Çukurova University, Adana-Turkey. She received her Master and PhD degrees (2018) in the same Faculties at Çukurova University.

Dr. Hippolyte AMAVEDA is an Assistant Professor at the University of Zaragoza and a member of the "Materials and laser treatments to improve energy efficiency" research group at ICMA (Institute of Materials Science of Aragon), Spain. His work deals with the synthesis and processing of materials, particularly complex oxides, using solid state and advanced routes. He is currently involved in projects developing new ceramic composite materials which are of interest for several multinational companies.

Dr. Héctor Santos Barahona received his MSc in Chemical Science and Technology and PhD in Advanced Chemistry at the University Complutense of Madrid. He has 10 years of experience in research, initially at Complutense University of Madrid and later in the Spanish National Research Council (CSIC-ICMA) in the field of material's corrosion protection and laser processing, respectively. He has been involved in applied research projects with private companies, as well as in publicly funded, national and EU projects, and is currently specialised in Laser Line Scan processing of surfaces.

Mr Carlos Borrel is a technician at the "Materials and laser treatments to improve energy efficiency" research group in the Aragón Institute for Materials Science (ICMA/University of Zaragoza-CSIC). He has expertise in electronics, having designed several electronic research instruments. During the last several years he has been involved in the development of new laser technologies for materials processing, based in Laser line scan melting techniques, as well as in LIFT and backwriting processes.

Prof. Sáez Puche received his Ph.D. from University Complutense of Madrid in 1979. He was associate Professor of Inorganic Chemistry (1985—99) and since 1999 he is Full Professor. He was a postdoctoral Fullbright Researcher at Arizona State University (USA) 1979—80, visiting Professor in the Department of Chemistry at UC Berkeley (2002),

CNRS-Paris (France), Poznan University (Poland), Ecole Superieure de Chimie (Strasbourg), Universidad Nacional de La Plata (Argentina) and Brunel University (UK). He was President of the Spanish Solid State Chemistry Group of the Spanish Royal Society of Chemistry (2009—2017) and member of the Board of the European Solid State Chemistry Group, as well as of the Board of College 5B at the ILL in Grenoble (2009—15). Since 1980 he has co-authored more than 300 publications, and delivered over 100 presentations as plenary, keynote and invited lectures in different international conferences. He has supervised 12 Doctoral Theses, and Leads the Solid State Chemistry Group at the University Complutense of Madrid since 2016.

Prof. Germán F. de la Fuente, Ph.D. in Chemistry is a Research Professor of the Spanish National Research Council (CSIC), working at the Aragón Institute for Materials Science (ICMA/University of Zaragoza-CSIC). He has specialised in developing surface coating and modification processing methods for ceramics, glasses, metals and C nanostructures. He has started the Laser Applications Laboratory at ICMA about 25 years ago, developing Laser induced Zone Melting methods to control solidification and microstructure in both, Superconductor and Eutectic Ceramics. He later established facilities for Laser Ablation of materials with the objective of developing original, large-area surface and coatings fabrication methods on metals, alloys, ceramics and glass, in addition to C nano-structure preparative techniques based on laser irradiation of graphitic and molecular precursors. His work has attracted attention from several industries, resulting in a large number of projects with Industrial partners at the local, national and European levels. He is the co-inventor of 10 patents and the coauthor of more than 150 scientific papers.

Prof. Luis A. Angurel is a Professor at the University of Zaragoza and researcher at the "Materials and laser treatments to improve energy efficiency" research group in the Aragón Institute for Materials Science (ICMA/University of Zaragoza-CSIC). From the point of view of materials processing, he has been working in the development of laser melting techniques to texture bulk High Temperature Superconductors and other ceramic materials with different cylindrical and planar geometries. In addition, he has developed laser ablation methods, as well as surface structuring and printing methodologies based on direct writing and LIFT (Laser Induced Forward Transfer) techniques. In the field of characterisation, his main area of research has been the development of thermal stability characterisation techniques for superconducting devices. In addition, he has been working in the development of several applications in the framework of research projects with different industrial companies. He has published over 100 papers in international journals, coordinated 15 research projects and has supervised 7PhD theses related with superconductivity and laser material processing.